Geoscientific
Model Development
Discussions

The GF Convection Parameterization: recent developments, extensions, and applications

Saulo R. Freitas[1,2], Georg A. Grell[3], and Haiqin Li[3,4]

[1]Goddard Earth Sciences Technology and Research, Universities Space Research Association, Columbia, MD, USA
[2]Global Modeling and Assimilation Office, NASA Goddard Space Flight Center, Greenbelt, MD, USA
[3]Earth Systems Research Laboratory of the National Oceanic and Atmospheric Administration, Boulder, CO, USA
[4]Cooperative Institute for Research in Environmental Sciences, University of Colorado Boulder, Boulder, CO, USA

Correspondence to: Saulo R. Freitas (saulo.r.freitas@nasa.gov)

Abstract. We detail recent developments in the GF (Grell and Freitas, 2014, Freitas et al., 2018) convection parameterization and applications. The parameterization has been extended to a trimodal spectral size to simulate the interaction and transition from shallow, congestus and deep convection regimes. Another main new feature is the inclusion of a closure for non-equilibrium convection that resulted in a substantial gain of realism in the simulation of the diurnal cycle of convection, mainly associated with boundary layer forcing over the land. Additional changes include the transport of momentum, the use of three Probability Density Functions (PDF's) to describe the normalized vertical mass flux profiles from deep, congestus, and shallow plumes (respectively) in the grid box, and the option of using temporal and spatial correlations to stochastically perturb PDF's, momentum transport and the closures. Cloud water detrainment is proportional to mass detrainment and in-cloud hydrometeor mixing ratio, and transport of chemical constituents (including wet deposition) can be treated inside the GF scheme. Transport is handled in flux form and is mass conserving. Finally, the cloud microphysics has been extended to include the ice phase to simulate the conversion from liquid water to ice in updrafts with resulting additional heating release, and the melting from snow to rain within a user-specified melting vertical layer.

1 Introduction

Convection Parameterizations (CPs) are sub-model components of atmospheric models that aim to represent the statistical effects of a sub-grid scale ensemble of convective clouds. It is necessary in models in which the spatial resolution is not sufficient to resolve the convective circulations. These parameterizations often differ fundamentally in closure assumptions and

parameters used to solve the interaction problem, leading to a large spread and uncertainty in possible solutions. For some interesting review articles on convective parameterizations the reader is referred to Frank (1984), Grell (1991), Emanuel and Raymond (1992), Emanuel (1994), and Arakawa (2004). A seminal work on CPs was done by Arakawa and Schubert

5   (1974). Following this, new ideas were implemented, such as including stochasticism (Grell and Devenyi, 2002, Lin and Neelin, 2003), and the super parameterization approach (Grabowski and Smolarkiewicz, 1999, Randall et al., 2003), to name a few.

An additional complication is the use of convective parameterizations on so-called "gray scales," which is gaining attention rapidly (Kuell et al., 2007, Mironov 2009, Gerard et al.,

10   2009, Yano et al., 2010, Arakawa et al., 2011, Grell and Freitas, 2014, Kwon and Hong, 2017). The original Grell and Freitas (2014, hereafter GF) scheme was built based on a convective parameterization developed by Grell (1993) and expanded by Grell and Devenyi (2002, hereafter GD) to include stochasticism by expanding the original scheme to allow for a series of different assumptions that are commonly used in convective parameterizations and that have

15   proven to lead to large sensitivity in model simulations. In GF, scale awareness (following Arakawa et al. 2011) was added for application on "gray scales", aerosol awareness was implemented by including a Cloud Condensation Nuclei (CCN) dependence of conversion from cloud water to rainwater in addition to using an empirical approach that relates precipitation efficiency to CCN. This version of GF is used operational in the Rapid Refresh

20   (RAP, Benjamin et al. 2016) at the Environmental Modeling Center (EMC) at the National Center for Environmental Prediction (NCEP) of the National Weather Service (NWS) in the US, at the Global Modeling and Assimilation Office of NASA Goddard Space Flight Center, and in the Brazilian Center for Weather Forecast and Climate Studies (CPTEC/INPE). Scale awareness was further tested successfully in GF, in a nonhydrostatic global model with

25   smoothly varying grid spacing from 50 to 3km (Fowler et al. 2016), and also in a cascade of global-scale simulations with uniform grid size spanning from 50 to 6 km using the NASA GEOS GCM (Freitas et al., 2018).

The use of GF in other modeling systems and for other applications required further modifications to represent physical processes such as momentum transport, cumulus congestus

30   clouds, modifications of cloud water detrainment, and better representation of the diurnal cycle of rainfall. In summary, the GF scheme has been evolved in several ways.

2

In Section 2, we will describe the new implementations, Section 3 will show some results from single column models to full 3D simulations, and Section 4 will conclude and summarize results.

2.1 The trimodal formulation

5   The unimodal deep plume has been replaced by a trimodal formulation, which allows up to three representations of plumes representing the main convective modes existing in a tropical environment (Johnson et al., 1999): shallow, congestus, and deep plumes. Each of the modes is distinguished by different lateral entrainment rates that strongly control its vertical depth and, consequently, the height of the main detrainment layers. Associated with each mode, a set

10   of closures to determine the mass flux at the cloud base were introduced to adequately account for the diverse regimes of convection in a given grid cell. The three modes transport momentum, tracers, water, and moist static energy. For mass and energy, the spatial discretization of the tendency equation is conservative on machine precision. The three modes are allowed to cohabit a given model grid column. The parameterization is performed over the

15   entire spectrum executing first the shallow representation, next the congestus, and finally the deep representation. In this manner, the convective tendencies resulting from the development of each mode can be applied as a forcing for the next one, if this approach is desired.

2.1.1 The shallow convection

The PDF for shallow convection represents continuous entraining-detraining vertical plumes,

20   with a large initial lateral entrainment rate (2.0 km^{-1}) at cloud base, with the cloud top constrained at the first inversion layer above the planetary boundary layer (PBL). Precipitation production can be turned on or off or can even be dependent on aerosol concentrations. For the results presented in this paper, we assume that shallow convection does not have enough vertical development to produce precipitation. So, the involved microphysics only allows water

25   at vapor and liquid (suspended) phases. The closures for the determination of the mass flux at cloud base, suitable for shallow moist convection regime, are as follows:

   – Raymond (1995), which establishes the equilibrium for the boundary layer budget of the moist static energy. In this case, the flux out at the cloud base of shallow convection counterbalances the flux in from surface process. This closure is called boundary layer

30   quasi-equilibrium (BLQE). The BLQE closure provides a reasonable diurnal cycle of shallow convection over land as the resulting mass flux at cloud base is tightly

connected with the surface fluxes. The equation for the mass flux at cloud base (m_b) from this closure reads

$$m_b = \frac{-\int_{p_s}^{p_{cb}} \frac{\partial \tilde{h}}{\partial t} \frac{dp}{g}}{(h_c - \tilde{h})_{cb}} \quad (1)$$

where h_c and $\tilde{h}$ are the in-cloud and environmental moist static energy, respectively, g is the gravity, p is the pressure, and the integral is determined from the surface to the cloud base. $\tilde{h}$ is approximated by the grid-scale moist static energy and its tendency is given by adding the tendencies from the grid-scale advection, diffusion in the planetary boundary layer (PBL) and radiation.

– Grant (2001), which introduced a closure based on the convective scale vertical velocity (w^*) PBL and the air density at the cloud base (ρ). In this closure, m_b is simply given by:

$$m_b = 0.03 \ \rho w^* \quad (2)$$

– Rennó and Ingersoll (1996) and Souza (1999), which applied the concept of convection as a natural heat engine to provide a closure for the updraft mass flux at cloud base:

$$m_b = \frac{\eta F_{in}}{TCAPE} \quad (3)$$

where η is the thermodynamic efficiency, F_{in} is the buoyancy surface flux and $TCAPE$ is the total convective available potential energy, which is approximated by the standard CAPE calculated from the vertical level of the air parcel source to the cloud top (Souza, 1999).

As an example of the performance of GF shallow scheme, we show in Figure 1 results obtained with the scheme implemented in the Brazilian developments on the Regional Atmospheric Modeling System (BRAMS, Freitas et al., 2017). The results correspond to a BRAMS simulation over the Amazon Basin on a horizontal grid spacing of 20 km and 2-day time integration, starting at 00UTC of 27 January 2014. The NCEP Global Forecast System analysis with 1° × 1° spatial resolution provided initial and boundary conditions for the meteorological fields. The diurnal cycle and vertical development of the PBL and the convective shallow are shown in Figure 1, using an average area of the turbulent kinetic energy and updraft mass flux as proxies. As the PBL gets deeper, the height of the maximum value of the mass flux profile consistently increases, realistically simulating a dry PBL capped by shallow cumulus, typical situation over the Amazon basin.

2.1.2 Congestus and deep convection

Congestus and Deep convection share several properties and will be described in this section. Both allow associated convective scale saturated downdraft as described in Grell (1993). As for shallow convection, they are distinguished by characteristic different initial gross

5 entrainment rate (0.9, 0.1 km^{-1}, respectively). The mass flux profiles are given by a Beta PDF, statistically representing the normalized statistical average mass flux of deep and congestus convection in a grid box. The effective vertical entrainment rate and detrainment rate profiles are derived from these mass flux profiles.

The closures formulations to determine the cloud base mass fluxes for deep convection are

10 described in GD. For congestus, the closures BLQE and based on W* described in Section 2.1.1 are available, besides the instability removal using a prescribed time scale.

2.2 Probability density functions representing the mass flux profiles

The original implementation of GF used a quadratic assumption for the normalized mass flux

15 to receive smooth profiles. The new version applies probability density functions (PDF) to represent the average statistical mass flux of the plumes, resulting in smooth normalized vertical mass flux profiles, providing an effective method to set the vertical distribution of heat and mass. We assume that the average normalized mass flux profiles for the updraft (Zu) and the downdrafts (Zd) may be represented with a Beta probability density function (PDF, see

20 en.wikipedia.org/wiki/Beta_distribution for further details). In this case, from determining the average cloud base and cloud top heights (two parameters), the profile can be analytically built with just one free parameter, which can be determined in terms of the desired shape and local of the maximum value of Zu or Zd. The normalized mass flux profile is then used to derive the average mass entrainment and detrainment over the layers.

25 For example, Figure 2 introduces the universe of solutions for Zu for a hypothetical case with cloud base at model level 5 and cloud top at level 50 in terms of the beta parameter values ranging from 1 to 6. An appropriate choice of the beta parameter implies on a profile smooth and deeper or sharp and shallower. There are two advantages to this representation of mass flux profiles are:

- Allows to set the average height of the mass flux maximum value as well as the heating and moistening tendencies. For example, for shallow convection the maximum should be located just above the planetary boundary layer. This also implies on a stronger coupling between the shallow convection and the boundary layer turbulence schemes.

5   – To smooth heating and moistening tendencies profiles, as a result from the analytical formulation being a smooth and continuous function, which is desirable for model stability and performance.

Figure 3 shows a representation by a beta PDF in the GF scheme of a mass flux profile obtained from large eddy simulations (Siebesma et al., 2003), LES, for undisturbed trade winds cumulus

10   convection under steady-state conditions. We note that the beta PDF representation of the LES profile is consistent, with a sharp increase starting from surface, peaking just above the boundary layer height, in this case approximately 1 km, and exhibiting a quasi-linear/smooth decrease above.

2.3 Diurnal cycle closure

15   Convection parameterizations based on the use of CAPE for closure and/or trigger function prove difficult in accurately representing the diurnal march of convection and precipitation associated with the diurnal surface heating in an environment of weak large-scale forcing. In nature, shallow and congestus convective plumes start a few hours after the sunrise, moistening and cooling the lower and mid-troposphere. This physical process prepares the environment

20   for the deep penetrative and larger rainfall producing convection sets in, which usually occurs in the mid-afternoon to early evening. Models, in general, simulate a more abrupt transition, with the rainfall peaking in phase with the surface fluxes, earlier than observations reveal.

In addition to a more accurate timing of the precipitation forecast, a realistic representation of the diurnal cycle in a global model also should improve the forecast of the near-surface

25   maximum temperature. Additionally, it improves the sub-grid scale convective transport of tracers, which should be especially relevant for carbon dioxide over vegetated areas. Moreover, as models configured in cloud-resolving scales can intrinsically capture the diurnal cycle of convection, global models with good skill on the diurnal cycle representation should yield a smoother transition from non-resolved to resolved scales. Lastly, it seems plausible that

30   benefits on the data assimilation are also expected with a better diurnal cycle representation.

In the attempt to improve the diurnal cycle in the GF scheme, we adopted a closure for non-equilibrium convection developed by Bechtold et al. (2014, hereafter B2014), which as we

Geoscientific
Model Development
Discussions

Open Access

EGU

further demonstrate, notably improves the simulation of the diurnal cycle of convection and precipitation over land. B2014 proposed the following equation for the convective tendency for deep convection which represents the stabilization response in the closure equation for the mass flux at cloud base:

5     $$\frac{\partial \Pi}{\partial t}\Big|_{conv} = -\frac{\Pi}{\tau} + \frac{\tau_{BL}}{\tau}\frac{\partial \Pi}{\partial t}\Big|_{BL} \qquad (4)$$

where Π is called density-weight buoyancy integral, and τ and τ_{BL} are appropriated time scales. The tendency of the second term on the right side of Eq. (4), is the total boundary layer production given by:

$$\frac{\partial \Pi}{\partial t}\Big|_{BL} = -\frac{1}{T^*}\int_{p_s}^{p_b}\frac{\partial \overline{T_v}}{\partial t}\Big|_{BL} dp \quad (5)$$

10   where the virtual temperature tendency includes tendencies from grid-scale advection, diffusive transport and radiation. T^* is a scale temperature parameter, and the integral is performed from the surface (p_s) to the cloud base (p_b). The justification for subracting a fraction of the boundary layer production is that Π already contains all the boundary layer heating but it is not totally available for deep convection.

15   While the impact for the GEOS modeling system was a substantial improvement, this may depend on other physical parameterizations and how tendencies are applied in a GCM. For this reason, in GF this closure is optional. On the other hand, it can be combined with any of the other closures previously available in the scheme for deep convection.

2.4 Inclusion of the ice phase process

20   The thermodynamical equation employed in GF scheme uses the moist static energy (h) as a conserved quantity for non-entraining air parcels with adiabatic displacements:

$$dh = 0 \ (6)$$

where h has the usual definition:

$$h = c_p T + gz + L_v q_v \ (7)$$

25   and c_p is the isobaric heat capacity of dry air, T is the temperature, g is the gravity, z is the height, L_v the latent heat of vaporization, and q_v the water vapor mixing ratio. However, h is not conserved if the glaciation transformation occurs, and this process was not explicitly included in GF until now. Incorporating the transformation of liquid water to ice particles, Eq. 6 now reads:

30    $$dh = L_f q_i \ (8)$$

7

where L_f is the latent heat of freezing, and q_i is the ice mixing ratio. With the extended Eq. 8, the general equation for the in-cloud moist static energy including the entraining process solved in this version of GF is

$$dh = L_f q_i + (dh)_{entr} \quad (9)$$

5   where $(dh)_{entr}$ represents the modification of the in-cloud moist static energy associated with the internal mixing with the entrained environmental air.

The partition between liquid and ice phases contents is represented by a smoothed Heaviside function which increases from 0 to 1 in the finite temperature range [250.16, 273.16] K.

The melting of precipitation across the freezing level is represented by adding an extra term to

10   the grid-scale moist static energy tendency:

$$\left(\frac{\partial \bar{h}}{\partial t}\right)_{melt} = -\frac{g\, L_f M}{\Delta p} \quad (10)$$

where M is the mass mixing ratio of the frozen precipitation that will melt in a given model vertical layer of the pressure depth Δp. The vertical range where melting is allowed is prescribed as residing in between $\pm$ 3K around the freezing level.

15   **3   Applications**

In this section, applications associated with novelties described in the previous section are discussed.

3.1 The trimodal characteristics revealed by single-column simulations

The GF convection scheme was implemented into the Global Model Test Bed (GMTB)

20   Single Column Model (SCM, https://dtcenter.org/GMTB/gmtb_scm_ccpp_doc/), and SCM simulations were executed using data from the Tropical Warm Pool International Cloud Experiment (TWP-ICE, May et al., 2008) to demonstrate the trimodal characteristics and the value of using PDF's. TWP-ICE is a comprehensive field campaign that took place on January and February 2006 over Darwin, Australia.

25   The time series of GF simulated total (red solid), convective (red dash) and observed total precipitation (black) are shown in Figure 4. Strong precipitation events are observed during the active monsoon period with a major Mesoscale Convective System (MCS) on 23 January 2006, and followed by a suppressed monsoon with relatively weak rainfall (Fig. 4). 19 January 2006 – 24 January 2006 and 26 January 2006 – 02 February 2006 are defined as active

30   monsoon and suppressed monsoon periods for the subsequent quantitative analysis. GF captures all the peak precipitation events during the active monsoon period. GF slightly

underestimates the heavy precipitation in the active monsoon period, and slightly overestimates the light precipitation evens in the suppressed monsoon period. The convective precipitation contributes about 78% of the total precipitation during the active monsoon period and contributes as high as 94% of total precipitation during the suppressed monsoon period.

5   To test the approximation of the normalized mass flux with our PDF approach, we compare the simulated mass flux profiles with observations, as analyzed by Kumar et al. (2016). Of particular importance for us is whether the PDF for deep convections is able to characterize deep convective clouds in the area, since this will determine maximum entrainment and detrainment in the parameterized clouds. For completeness we also compare

10   congestus and shallow clouds. The mean mass flux during the whole TWP-ICE simulation period from all cumulus clouds (deep, congestus, and shallow), congestus, and deep convection are shown in Figure 5. The congestus mass flux (green), which is weaker than the mass flux for deep convection, has the cloud top around 7 km height. The maximum mass flux from deep convection (red) and all convective types (black) is around 6km and a bit under 6km,

15   respectively. Kumar et al. (2016) estimated the convective mass flux from two wet season (October 2005 – April 2006 and October 2006 – April 2007) from radar observations over Darwin, Australia. Although the TWP-ICE simulation period is much shorter, the shape of mass flux profiles in Figure 5 is quite similar to their observations (Figure 13 of Kumar et al. 2016).

20   Figure 6 presents the averaged updraft mass flux, downdraft mass flux in active and suppressed monsoon periods for shallow, congestus, and deep convection. The maximum updraft mass flux for shallow, congestus and deep convection is at around 850hPa, 750hPa and 500hPa respectively, while the maximum downdraft mass flux is found near the surface for both congestus and deep convection. As expected, the updraft and downdraft mass flux are

25   stronger in the active monsoon period than in the suppressed monsoon period. Other observational comparisons (Mrowiec et al., 2012; Kumar et al., 2015; Kumar et al., 2016) showed updraft and downdraft mass flux profiles of similar characteristics.

        Figure 7 shows the convective heating rate of shallow (Fig. 7a), congestus (Fig. 7b), and deep convection (Fig. 7c). In the case of the shallow convection (Fig. 7a) the environment

30   is warmed in the lower levels, and cooled by the evaporation of the detrained liquid water at cloud tops. The shallow heating by shallow convection appears more active in the monsoon stage. The congestus (Fig. 7b) and deep (Fig. 7c) convection cool the boundary layer mainly by downdrafts and evaporation of rainfall, and also cool the troposphere by the evaporation of

9

the detrained condensates at cloud tops. On 23 January 2006, the strong heating from lower troposphere to 500hP and 200hPa for congestus and deep convection, respectively, corresponds to the heavy precipitation in Figure 4. Figure 8 shows the convective drying tendencies of shallow (Fig. 8a), congestus (Fig. 8b) and deep convection (Fig. 8c). The entraining of low-

5 level environmental moist air into the convection plumes and raining out results in drying of low-level atmosphere, while the detrained cloud water/ice moistens the cloud top of all kind of parameterized convective clouds. The strongest drying for deep convection on 23 January 2006 (Fig. 8c) from lower troposphere to 200hPa also corresponds to the heavy precipitation in Figure 4.

10 **3.2) Evaluation of the Diurnal Cycle Closure**

Santos e Silva et al. [2009, 2012] discussed in detail the diurnal cycle of precipitation over the Amazon Basin using the TRMM rainfall product (Huffman et al., 2007) and observational data from an S-band polarimetric radar (S-POL) and rain gauges obtained in a field experiment during the wet season of 1999. Their analysis indicated that the

15 peak in rainfall is usually late in the afternoon (between 17:00 and 21:00 UTC), despite existent variations associated with wind regimes. In addition, over the Amazon, a secondary convection activity is observed during the nocturnal period as reported by Yang et al. (2008) and Santos e Silva et al. (2012); in general, this is associated to squall lines propagation in the Amazon basin (Cohen et al., 1995; Alcantara et al., 2011). This

20 bimodal pattern of convective activity can be identified with observational analysis of vertical profiles of moistening and heating (Schumacher et al., 2007).

Here we evaluate the GF scheme with the B2014 closure, applying it with the NASA GEOS GCM configured as a single column model (SCM). GEOS with GF was run as a SCM from 24 January to 25 February 1999 using the initial condition and advective

25 forcing from the TRMM_LBA field campaign data. Model results were averaged in time in order to express the mean diurnal cycle. Figure 9 shows the mean diurnal cycle of the vertical mass flux from shallow, congestus and deep convection, as well as the total and convective precipitation. In this figure, each type of convection is depicted with a specific uniform color which define its spatial and temporal evolution. The

30 uniform shaded areas denote values that are at least 5% of the maximum value of mass

10

flux of each type of parameterized convection. The chosen closures for the average mass flux at cloud base were the BLQE for shallow and the B2014 for congestus and deep convection. For congestus, we only retained the first term of Equation 4; for deep, the simulations were performed without and with the second term of Equation 4. This allowed us to evaluate its role on defining the phase of the diurnal march of the precipitation.

Panel (A) of Figure 9 shows the model results without applying the diurnal cycle closure (i.e. retaining only the first term of Equation 4) for deep convection. In this case, the three convective modes coexist, triggered just a few hours after the sunrise (~11 UTC), with the deep convection occurring too early and producing a maximum precipitation of about 15 UTC (~11 Local Time). Conversely, we observed a clear separation between the convective modes when applying the full equation of the diurnal cycle closure (Panel B), reducing the amount of potential instability available for the deep convection. In this case, there is a delay of the precipitation from the deep penetrative convection with the maximum rate taking place between 18 and 21 UTC, more consistent with observations of the diurnal cycle over the Amazon region.

Figure 10 introduces the grid-scale vertical moistening (on the left) and heating (on the right) tendencies associated with the three convective modes for the simulations with- out and with the diurnal cycle closure. The net effect (moistening minus drying) of the three convective modes, not including the diurnal cycle closure for the deep mode, appears in the Panel (A). As the three modes co-exist most of the time and as the drying associated with the deep precipitating plumes dominates, water vapor is drained from the troposphere, with a shallow lower-level layer of moistening associated with the precipitation evaporation driven by the downdrafts. However, by including the full formulation of the diurnal cycle closure (Panel B), a much smoother transition is simulated with a late morning and early afternoon low/mid-tropospheric moistening by shallow and congestus convection, followed by a late afternoon and early evening tropospheric drying by the rainfall from the deep cumulus. Associated with the delay of precipitation, the peak of downdrafts occurrence is correspondingly displaced. On the right, Panels C and D introduce the results for the heating tendencies. A similar discussion applies to these tendencies, with the peak of the atmospheric heating delayed by a few hours,

11

when the diurnal cycle closure is applied (Panel D). Note, the warming from the congestus plumes some- what offsets the low-troposphere cooling associated with the shallow plumes.

3.3 Global Scale Modeling

A global scale evaluation of the diurnal cycle closure is shown in this section applying GF

5   within the NASA GEOS GCM model (Molod et al., 2015). The GEOS GCM was configured with c360 spatial resolution ($\sim 25km$) and was run in free forecast mode for all of January 2016. Each forecast day comprised a 120-h time integration, with output available every hour. Atmospheric initial conditions were provided by the Modern–Era Retrospective Analysis for Research and Applications, Version 2 (MERRA–2, Gelaro et al., 2017). The simulations

10   applied the non-hydrostatic dynamical core FV3 (Putman et al., 2007) and the single-moment version of the microphysics scheme (Bacmeister et al., 2006). The longwave radiative processes are represented following Chou and Suarez (1994), and the shortwave radiative processes are from Chou and Suarez (1999). The turbulence parameterization is a non-local scheme primarily based on Lock et al. (2000), acting together with the local first order scheme

15   of Louis and Geleyn (1982). The sea surface temperature is prescribed following Reynolds et al. (2002).

We first demonstrate the impact of the boundary layer production on the cloud work function (CWF) available for the deep convection overturning. In GF, CWF is calculated as

$$A = \int_{zb}^{zt} \frac{g}{c_p \bar{T}} \frac{\eta}{1+\gamma} (h_u - \bar{h}) \, dz \quad (11)$$

20   where, A is the total updraft CWF, z_b and z_t are the height of the cloud base and cloud top, respectively, g is the gravity, c_p the specific heat of dry air, η is normalized mass flux, $\bar{T}$ is the grid-scale temperature, and h_u, $\bar{h}$ are the updraft and grid-scale moist static energy, respectively. The parameter γ is given by Grell (1993, Eq. A15). Following B2014, the boundary layer production is given by:

25   $$A_{BL} = -\frac{\tau_{BL}}{T^*} \int_{p_{surf}}^{p_{base}} \frac{\partial \overline{T_v}}{\partial t}\bigg|_{BL} \rho \, dp \quad (12)$$

where ρ is the air density and the integral being performed from the surface to the cloud base. From Equations 11 and 12, the available CWF (A_{avail}) is given by

$$A_{avail} = A - A_{BL} (13)$$

Figure 11 shows the monthly mean of the diurnal variation of the three quantities given by Eqs.

30   11, 12 and 13. The figure represents the monthly mean (January 2016) of the diurnal variation

of the total cloud work function, boundary layer production, and the available cloud work function all areal-averaged over the Amazon region.

The total CWF tightly follows the surface fluxes as the air parcels that form the convective updrafts originate close to the surface in the PBL. The boundary layer production presents

5   similar behavior, peaking at noon and developing negative values during the nights. The combination of the two terms following the Eq. (13) defines the available CWF for convection overturning. Note, a negative range of the available CWF in the early mornings to approximately noon, prevents the model from developing convective precipitation in that period and shifting the maximum CWF to late afternoon, much closer to the observed diurnal

10   cycle of precipitation over the Amazon region.

A global view of these three quantities is shown in Figure 12. As before, the curves represent the monthly mean (January 2016) of the diurnal variation of the total cloud work function, boundary layer production, and the available cloud work function. Here the averaged areal corresponds to the global domain (panel A), only the land regions (panel B) and only the oceans

15   (panel C). Over oceans, the boundary layer production is small in comparison with the total CWF, and does not do much; instead, over land (panel B), it is comparable in magnitude with the total CWF, pushing the available CWF to peaks closer to the late afternoons and early evenings. On global average (panel A), the boundary layer production still plays a substantial role with a clear effect in the timing of the maximum available CWF.

20   A global perspective of the precipitation simulation with GEOS GCM with the GF scheme and the impact of the diurnal cycle closure is provided by Figure 13. Here, the January 2016 average of the diurnal cycle of the precipitation over land (right column) and oceans (left columns) areas are depicted as estimated by the TRMM Multi-satellite Precipitation Analysis (TMPA version 3B42, Huffman et al. (2007), upper panels, A and D) and simulated by the GEOS-GF,

25   including (at middle, panels C and E) or not (lower panels, D and F) the diurnal cycle closure. The precipitation field was further averaged over the latitudes 40 S and 40 N, and the vertical axis represents the local time. TRMM estimation evidences two peaks of precipitation: a nocturnal one around 3 AM over oceans and another one in late afternoon (3 to 6 PM) over land. A significant gap of rainfall between 6 AM and noon is also seen. Both simulations with

30   model GEOS-GF seem to perform well regarding the precipitation amount, mainly over the oceans (right column). As expected from the previous discussion about the time variability of the available CWF over the oceans, both simulations (panels E and F) show a similar diurnal

cycle of the precipitation, being very close with the observations made by the TRMM (panel D).

Over land domains (left column), we found a somewhat overestimation of the precipitation in comparison with the estimates produced by the TRMM retrieval technique (panel A). However, the simulation that applies the diurnal cycle closure (panel B) is superior regarding the phase in comparison with the simulation which applies the total CWF (panel C) for the closure. As shown in panel B, the diurnal cycle closure used in this simulation shows a much better representation of the morning to early afternoon gap of the precipitation, which peaks much closer to the time of TRMM observation. In particular, model improvements are noticeable over the Amazon region (denoted by "SA" in panel A). Similar improvements are also evident over Africa ("AFR") and Australia ("AUS").

4 Conclusions

We describe a set of new features recently implemented in the GF convection parameterization. The main new aspects are as follows

- The unimodal approach has been replaced by a trimodal formulation representing the three modes: shallow, congestus, and deep convection. Each mode has a distinct initial gross entrainment and a set of closure formulations for the mass flux at the cloud base.

- The normalized mass flux profiles are now prescribed following a continuous and smooth probability density function. From the cloud base, cloud top, and a free parameter, which molds the PDF, the normalized mass flux profile, the entrainment and detrainment rates are determined. Together with the mass flux at the cloud base defined by the selected closure, they also determine, e.g., the vertical drying and heating tendencies associated with the sub-grid-scale convection. This approach allows for fine-tuning in the model skill by guiding on the water vapor and temperature biases. Besides and perhaps more importantly, it can be used to implement stochasticism with temporal and spatial correlations and memory dependence that lead to significant changes in the vertical distribution of heating

and drying without disturbing mass conservation. Future work will address this possibility.

- An optional closure for non-equilibrium convection (Bechtold et al., 2014) is available. This closure has shown a significant gain of the GF scheme's ability in NASA GEOS GCM in representing the diurnal cycle of convection over land, with impacts also in data assimilation and tracer transport.

We understand that the previous GF scheme's features with the new ones described in this paper, further extends the capabilities of this convection parameterization to be applied in a wide range of spatial scales and environmental problems.

Code availability

The GF convection scheme is avalaible in the Global Model Test Bed (GMTB) Single Column Model (SCM, https://dtcenter.org/GMTB/gmtb_scm_ccpp_doc/). Public access to the NASA GEOS GCM source code is available at github.com/GEOS- ESM/GEOSgcm on tag Jason-3 0. The authors are available for recommendations of the applying the several options present in the GF scheme. Also, for instructions related to its implementation in other modeling systems.

Competing interests

The authors declare that they have no conflict of interest.

Author contribution

SRF and GAG developed the model code and performed the simulations. HL conduced the simulations shown in Section 3.1.1. All authors prepared the manuscript.

Acknowledgements

References

Arakawa, A., & Schubert, W. H.: Interaction of a cumulus cloud ensemble with the large-scale environment, Part I. J. Atmos. Sci., 31, 674–701, doi:10.1175/1520- 0469, 1974.

Arakawa, A., Jung, J.-H., & Wu, C.-M.: Toward unification of the multiscale modeling of the atmosphere. Atmos. Chem. Phys., 11, 3731–3742, doi:10.5194/acp- 11-3731-2011, 2011.

Alcantara, C. R., Silva Dias, M. A. F., Souza, E. P., & Cohen, J. C. P.: Verification of the role of the low-level jets in Amazon squall lines, J. Atmos. Res., 100:36–44. doi: 10.1016/j.atmosres.2010.12.023, 2011.

Bacmeister, J. T., Suarez, M. J., and Robertson, F. R.: Rain reevaporation, boundary layer-convection interactions, and Pacific rainfall patterns in a AGCM, J. Atmos. Sci., 63, 3383–3403, 2006.

Bechtold, P., N. Semane, P. Lopez, J. Chaboureau, A. Beljaars, and N. Bormann: Representing Equilibrium and Nonequilibrium Convection in Large-Scale Models. J. Atmos. Sci., 71, 734–753, doi: 10.1175/JAS-D-13-0163.1, 2014.

Chou, M.-D. and Suarez, M. J.: An efficient thermal infrared radiation parameterization for use in general circulation models. NASA Tech. Memorandum 104606 – Vol. 3, NASA, Goddard Space Flight Center, Greenbelt, MD, 1994.

Chou, M.-D. and Suarez, M. J.: A Solar Radiation Parameterization for Atmospheric Studies. NASA Tech. Memorandum 104606 – Vol. 15, NASA, Goddard Space Flight Center, Greenbelt, MD, 1999.

Cohen, J. C. P., Silva Dias, M. A. F., & Nobre, C. A.: Environmental conditions associated with Amazonian squall lines: a case study. Monthly Weather Review, 123: 3163-3174, 1995.

Freitas, S. R., Panetta, J., Longo, K. M., Rodrigues, L. F., Moreira, D. S., Rosário, N. E., Silva Dias, P. L., Silva Dias, M. A. F., Souza, E. P., Freitas, E. D., Longo, M., Frassoni, A., Fazenda, A. L., Santos e Silva, C. M., Pavani, C. A. B., Eiras, D., França, D. A., Massaru, D., Silva, F. B., Santos, F. C., Pereira, G., Camponogara, G., Ferrada, G. A., Campos Velho, H. F., Menezes, I., Freire, J. L., Alonso, M. F., Gácita, M. S., Zarzur, M., Fonseca, R. M., Lima, R. S., Siqueira, R. A., Braz, R., Tomita, S., Oliveira, V., and Martins, L. D.: The Brazilian developments on the Regional Atmospheric Modeling System (BRAMS 5.2): an integrated environmental model tuned for tropical areas, Geosci. Model Dev., 10, 189-222, doi:10.5194/gmd-10-189-2017, 2017.

Freitas, S. R., Grell, G. A., Molod, A., Thompson, M. A., Putman, W. M., Santos e Silva, C. M., & Souza, E. P.: Assessing the Grell-Freitas convection parameterization in the NASA GEOS modeling system. Journal of Advances in Modeling Earth Systems, 10, 1266–1289. https://doi.org/10.1029/2017MS001251, 2018.

16

Gelaro, R., W. McCarty, M.J. Suarez, R. Todling, A. Molod, L. Takacs, C.A. Randles, A. Darmenov, M.G. Bosilovich, R. Reichle, K. Wargan, L. Coy, R. Cullather, C. Draper, S. Akella, V. Buchard, A. Conaty, A.M. da Silva, W. Gu, G. Kim, R. Koster, R. Lucchesi, D. Merkova, J.E. Nielsen, G. Partyka, S. Pawson, W. Putman, M. Rienecker, S.D. Schubert,

5   M. Sienkiewicz, and B. Zhao: The Modern–Era Retrospective Analysis for Research and Applications, Version 2 (MERRA–2). J. Climate, 30, 5419–5454, https://doi.org/10.1175/JCLI–D–16–0758.1, 2017.

Grell, G. A. and Devenyi, D.: A generalized approach to parameterizing convection combining ensemble and data assimilation techniques, Geoph. Res. Let., 29, 38-1–38-4,

10   doi:10.1029/2002GL015311, 2002.

Grell, G. A. and Freitas, S. R.: A scale and aerosol aware stochastic convective parameterization for weather and air quality modeling, Atmos. Chem. Phys., 14, 5233-5250, doi:10.5194/acp-14-5233-2014, 2014.

Huffman, G. J., Adler, R. F., Bolvin, D. T., Gu, G. J., Nelkin, E. J., Bowman, K. P., Hong, Y.,

15   Stocker, E. F., and Wolff, D. B.: The TRMM multi-satellite precipitation analysis (TMPA): Quasi-global, multiyear, combined-sensor precipitation estimates at fine scales. J. of Hydrometeo., 8, 38-55. 2007.

Johnson, R.H., T.M. Rickenbach, S.A. Rutledge, P.E. Ciesielski, and W.H. Schubert: Trimodal Characteristics of Tropical Convection. J. Climate, 12, 2397–2418, doi: 10.1175/1520-0442,

20   1999.

Kumar, V. V., C. Jakob, A. Protat, C. R. Williams, and P. T. May: Mass-Flux Characteristics of Tropical Cumulus Clouds from Winder Profiler Observations at Darwin, Australia. J. Atmos. Sci, 72, 1837-1855, 2015.

Kumar, V. V., A. Protat, C. Jakob, C. R. Williams, S. Rauniyar, G. L. Stephens, and P. T. May:

25   The Estimation of Convective Mass Flux from Radar Reflectivities. J. Appl. Meteor. Climatol., 55, 1239-1257, 2016.

Kwon, Y. C., & Hong, S.-Y.: A Mass-Flux cumulus parameterization scheme across gray-zone resolutions. Monthly Weather Review, 145, 583–598. https://doi.org/10.1175/MWR-D-16-0034.1, 2017.

30   Lock, A. P., Brown, A. R., Bush, M. R., Martin, G. M., and Smith, R. N. B.: A new boundary layer mixing scheme. Part I: Scheme description and single-column model tests, Mon. Weather Rev., 138, 3187–3199, 2000.

Louis, J. & Geleyn, J.: A short history of the PBL parameterization at ECMWF. Proc. ECMWF Workshop on Planetary Boundary Layer Parameterization, Reading, United Kingdom, ECMWF, 5980, 1982.

May, T. P., J. H. Mather, G. Vaughan, C. Jakob, G. M. McFarquhar, K. N. Bower, and G. G. Mage: The Tropical Warm Pool International Cloud Experiment. Bull. Amer. Meteor. Soc., 89, 629-645, 2008.

Molod, A., Takacs, L., Suarez, M., and Bacmeister, J.: Development of the GEOS-5 atmospheric general circulation model: evolution from MERRA to MERRA2, Geosci. Model Dev., 8, 1339-1356, doi:10.5194/gmd-8-1339-2015, 2015.

Mrowiec, A. A., C. Rio, A. M. Fridlind, A. S. Ackerman, A. D. Del Genio, O. M. Pauluis, A. C. Varble, and J. Fan: Analysis of cloud-resolving simulations of a tropical mesoscale convective system observed during TWP-ICE: Vertical fluxes and draft properties in convective and stratiform regions. J. Geophys. Res., 117, D19201, doi:10.1029/2012JD017759, 2012.

Putman, W. and Lin, S.-J.: Finite Volume Transport on Various Cubed Sphere Grids. J. Comput. Phys., 227, 55–78. doi:10.1016/j.jcp.2007.07.022, 2007.

Raymond, D. J.: Regulation of moist convection over the west pacific warm pool. J. Atmos. Sci., 52, 3945–3959, 1995.

Rennó, N. and A. P. Ingersoll: Natural convection as a heat engine: A theory for CAPE.J. Atmos. Sci., 53, 572–585, 1996.

Reynolds, R. W., Rayner, N. A., Smith, T. M., Stokes, D. C., and Wang, W.: An improved in situ and satellite SST analysis for climate, J. Climate, 15, 1609–1625, 2002.

Santos e Silva, C. M., Gielow, R. and Freitas, S. R.: Diurnal and semidiurnal rainfall cycles during the rain season in SW Amazonia, observed via rain gauges and estimated using S-band radar. Atmosph. Sci. Lett., 10: 87–93. doi: 10.1002/asl.214, 2009.

Santos e Silva, C. M., Freitas, S. R., Gielow, R.: Numerical simulation of the diurnal cycle of rainfall in SW Amazon basin during the 1999 rainy season: the role of convective trigger function. Theoretical and Applied Climatology, 109, 473-483, 2012.

Schumacher, C., Zhang, M. H., & Ciesielski, P.E.: Heating Structures of the TRMM Field Campaigns. J. Atmos. Sci., 64: 2593–2610. DOI: 10.1175/JAS3938.1, 2007.

Siebesma, A.P., C.S. Bretherton, A. Brown, A. Chlond, J. Cuxart, P.G. Duynkerke, H. Jiang, M. Khairoutdinov, D. Lewellen, C. Moeng, E. Sanchez, B. Stevens, and D.E. Stevens: A Large Eddy Simulation Intercomparison Study of Shallow Cumulus Convection. J. Atmos.

Sci.,   60,   1201–1219,   https://doi.org/10.1175/1520-0469(2003)60<1201:ALESIS>2.0.CO;2, 2003.

Souza, E. P.: Estudo Teórico e Numérico da Relação entre Convecção e Superfícies Heterogêneas na Região Amazônica, Ph.D. thesis, São Paulo University, São Paulo, SP, Brazil, 1999 (in Portuguese).

Yang, S., Kuo, K.S., & Smith, E.A: Persistent Nature of Secondary Diurnal Modes of Precipitation over Oceanic and Continental Regimes. Journal of Climate, 21: 4115– 413. doi: 10.1175/2008JCLI2140.1, 2008.
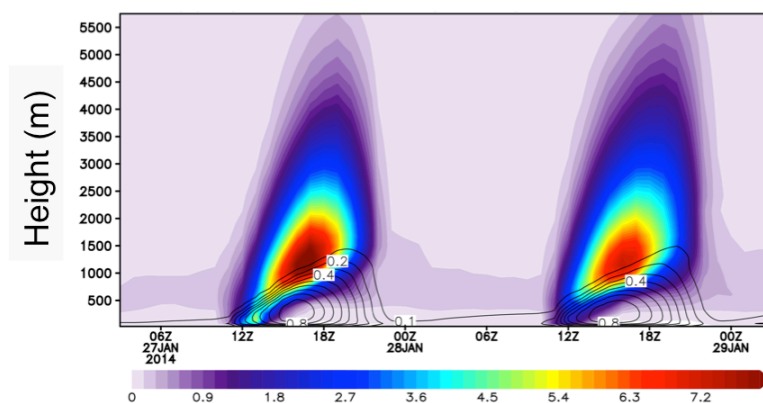
5 **Figures**

Figure 1. Diurnal cycle of the turbulent kinetic energy (TKE, $m^2 s^{-2}$, black contours), as a proxy of PBL; and the mass flux ($10 kg m^{-2} s^{-2}$, shaded colors), as a proxy for the shallow convection

10   with saturated air. The results correspond to an average area in the Amazon Basin in the model domain.
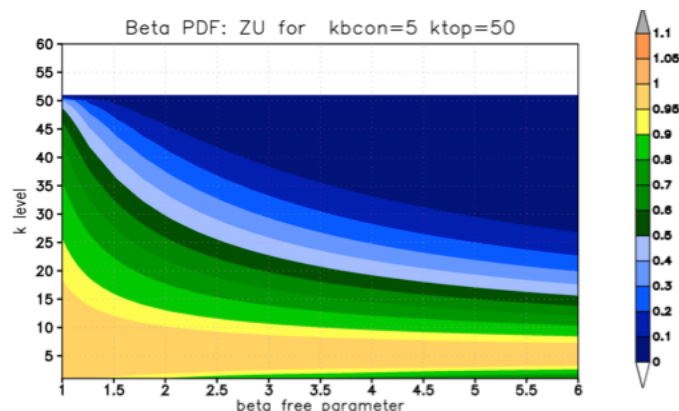
Figure 2. The universe of solutions for the normalized updraft mass flux profile for a cloud base at a generic vertical level 5 and cloud top at level 50 in terms of a beta parameter varying from 1 to 6.

5
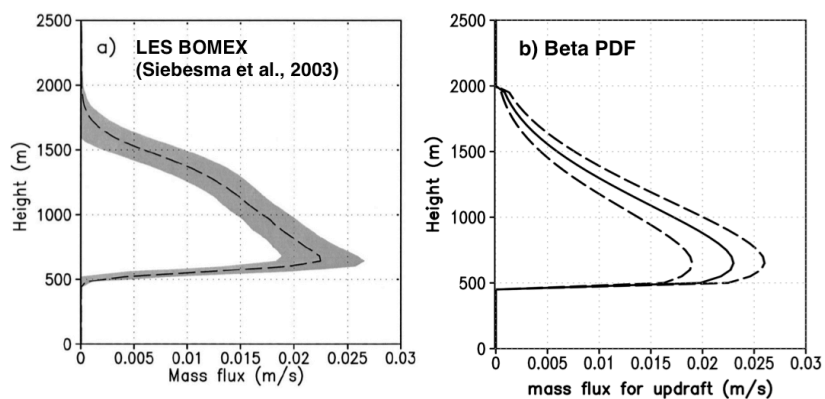
Figure 3. On the left, mass flux profile of shallow convection simulated by a large eddy resolving model (Siebesma, A.P., C.S. Bretherton, A. Brown, et al.: A Large Eddy Simulation Intercomparison Study of Shallow Cumulus Convection. J. Atmos. Sci., 60, 1201–1219, 2003. © American Meteorological Society. Used with permission.) On the right, a representation of the mass flux profile within the GF convection parameterization.

10

15

21
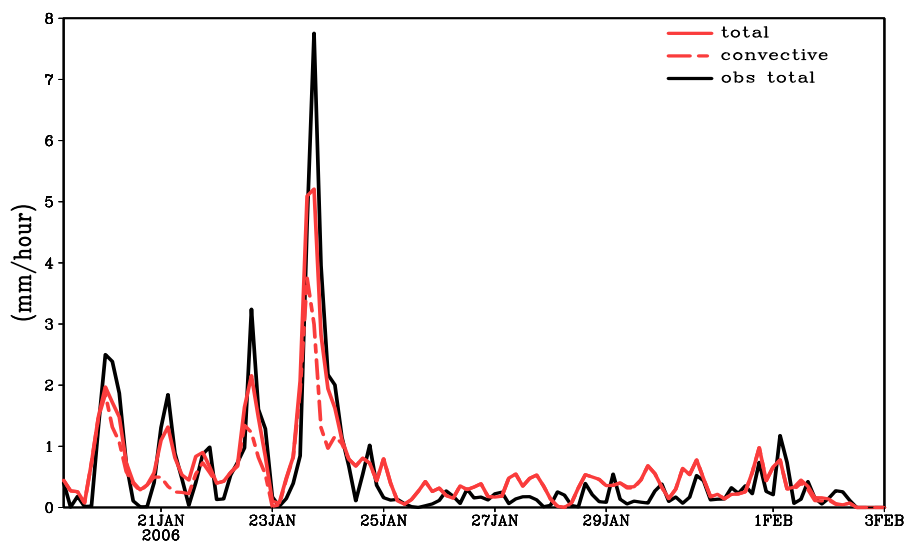
Figure 4. Total (red solid), convective (red dashed) and observed total precipitation rates (mm/hour) with GF scheme using the TWP-ICE soundings.

5
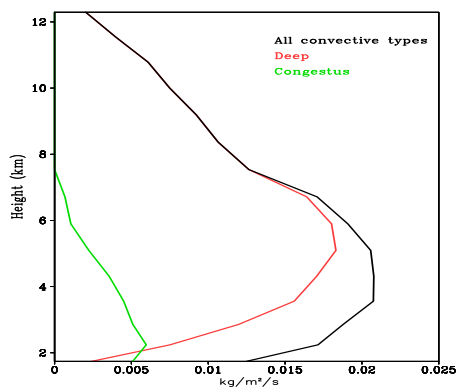
Figure 5. The TWP-ICE mean mass flux ($kg\ m^2\ s^{-1}$) profiles from all cumulus clouds (in black), congestus (in green), and deep convection (in red).

22
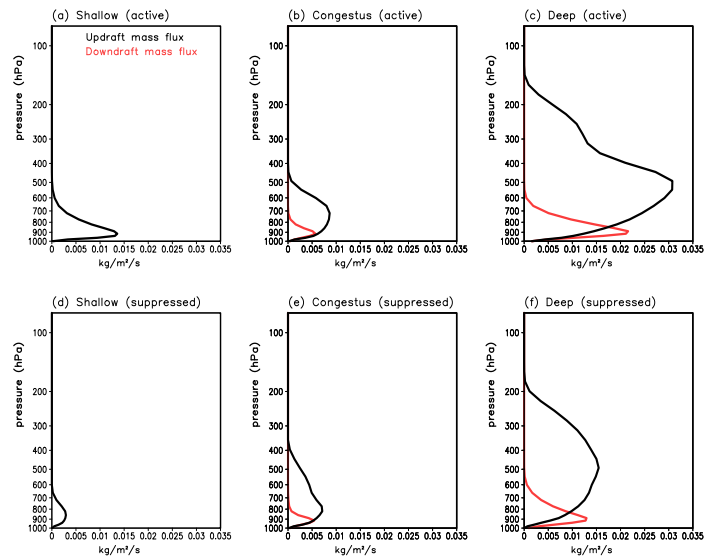
Figure 6. The averaged mass flux ($kg\ m^2\ s^{-1}$) profiles of updraft mass flux (in black), and downdraft mass flux (in green) in active monsoon period for the (a) shallow, (b) congestus, (c) deep convection, and in suppressed monsoon period for the (d) shallow, (e) congestus, (f) deep convection.
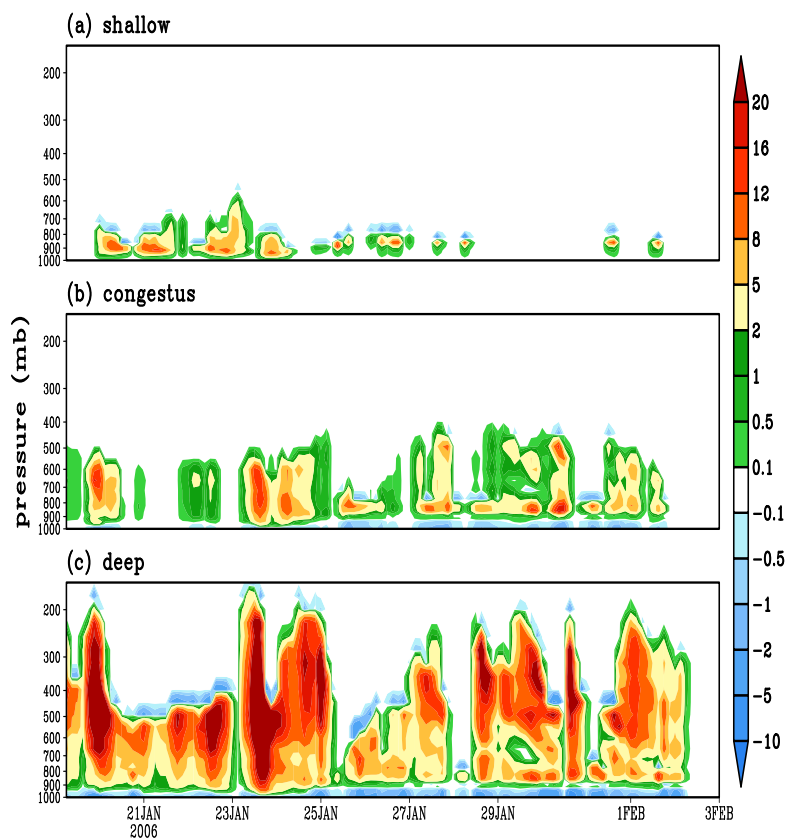
Figure 7. Convective heating tendencies (K/day) of (a) shallow, (b) congestus, and (c) deep convection with GF scheme using the TWP-ICE soundings.
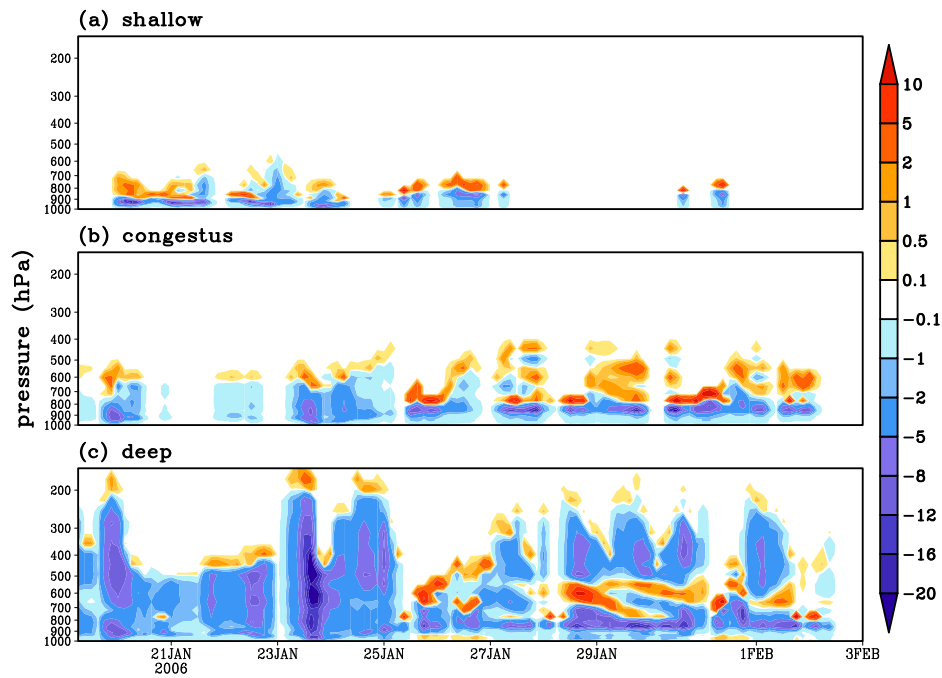
Figure 8. Convective drying tendencies (g/Kg/day) of (a) shallow, (b) congestus, and (c) deep convection with GF scheme using the TWP-ICE soundings.
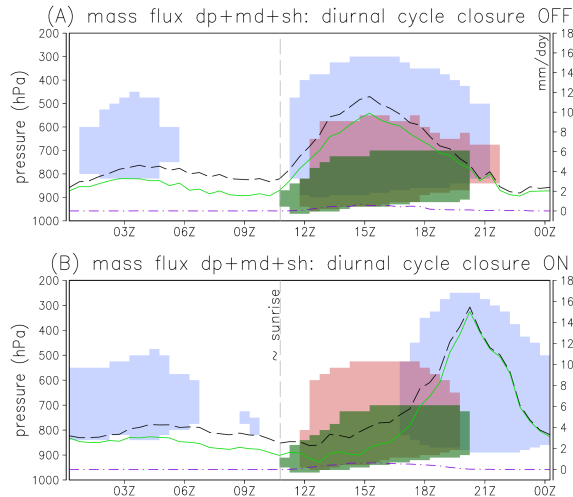
Figure 9. Time average of the diurnal cycle of the vertical mass flux of the three convective modes (shaded: green, light red, and light blue represents shallow, congestus, and deep, respectively) and precipitation (contour: black dash, green solid and purple dash represents the total precipitation, and the convective part from deep and congestus plumes, respectively). The scale for precipitation appears on the right axis in mm/day. Panel A (B) represents the results without (with) the diurnal cycle closure.
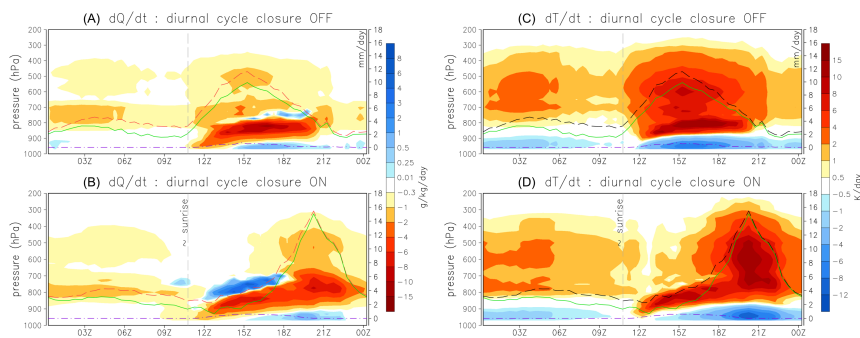
Figure 10. Time average of the diurnal cycle of the grid-scale vertical moistening (left) and heating (right) tendencies associated with the three convective modes (shaded colors) and precipitation (contour: red dash, green solid and purple dash represents the total precipitation, and the convective precipitation from deep and congestus plumes, respectively). The upper (bottom) panels show results without (with) the diurnal cycle closure.

26
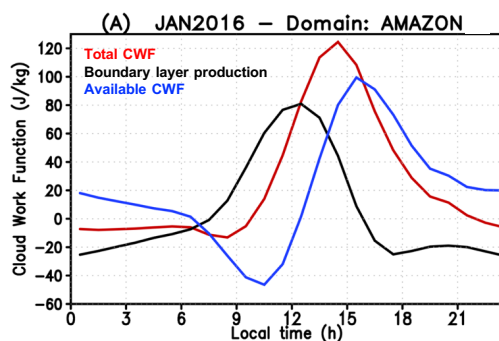
Figure 11. The monthly mean (January 2016) of the diurnal variation of the total cloud work function (red color), boundary layer production (black) and the available cloud work function (blue). The curves also represent the areal average over the Amazon region.

5
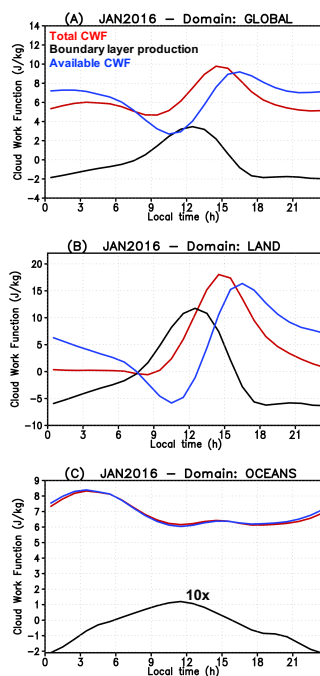
Figure 12. The monthly mean (January 2016) of the diurnal variation of the total cloud work function (red color), boundary layer production (black) and the available cloud work function (blue). The curves also represent the areal average over (A) the entire world, (B) the land regions, and (C) the oceans. In panel (C) the boundary layer production is multiplied by 10 for clarity.

10

27
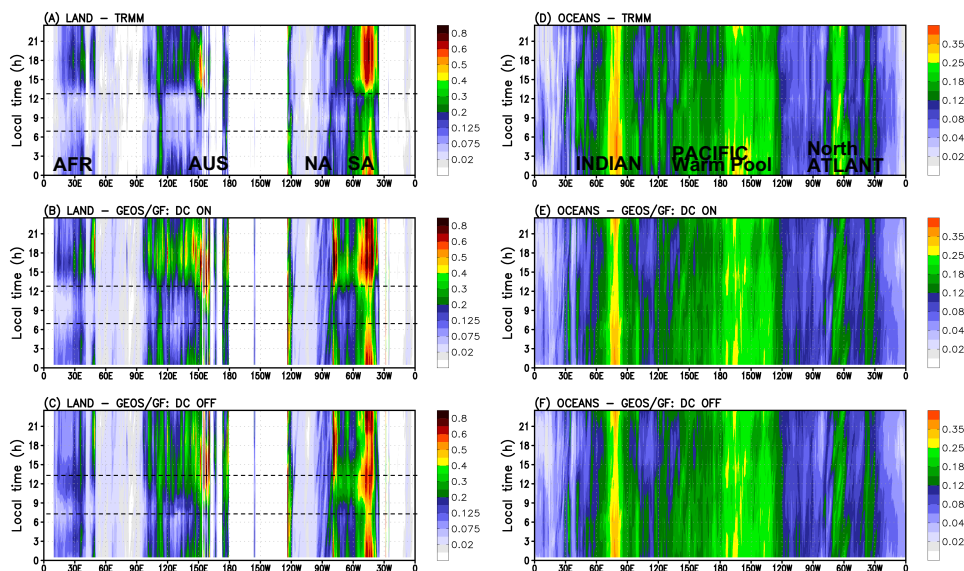
Figure 13. Global Hovmöller Diagram (average over latitudes 40S to 40N) of the diurnal cycle of precipitation (mm h^{-1}) from remote sensing-derived observation (TRMM, upper panels) and

5   NASA GEOS GCM applying the GF scheme with the diurnal cycle closure (middle panels, DC ON) and without (lower panels, DC OFF). The results are for January 2016 grouping only over land (left column) and the oceans (right column) regions, respectively. Note that the color scales are different for ocean and land panels.